



CrossMark
click for updates

Cite this: *RSC Adv.*, 2016, 6, 29371

Activity and kinetics of ruthenium supported catalysts for sodium borohydride hydrolysis to hydrogen†

Yunhua Li,^{*a} Xing Zhang,^a Qi Zhang,^a JinBao Zheng,^a NuoWei Zhang,^a Bing H. Chen^a and K. J. Smith^b

Ru–RuO₂/C prepared by galvanic replacement has high catalytic activity for sodium borohydride hydrolysis. In the present study, a series of Ru–RuO₂/C catalysts, Ru–RuO₂/C reduced, RuO₂/C and Ru supported on Ni foam (Ru/Ni foam) are prepared and characterized. Results show that RuO₂ on Ru–RuO₂/C is formed from both the consumption of the parent Ni and NiO nanoparticles and the disproportionation of RuCl₃ with epitaxial growth of Ru species. The quantity of RuO₂ with oxygen vacancies in Ru–RuO₂/C determines the hydrolysis activity for sodium borohydride. In contrast to Ru–RuO₂/C, Ru/Ni foam without oxygen vacancies has the lower hydrolysis activity. Results of kinetics calculation further confirm that without mass transfer limitation, Ru–RuO₂/C has lower intrinsic activation energy and correspondingly higher catalytic activity due to existence of oxygen vacancies than those from Ru–RuO₂/C reduced, RuO₂/C, Ru/Ni foam and catalysts from the literature.

Received 10th January 2016

Accepted 12th March 2016

DOI: 10.1039/c6ra00747c

www.rsc.org/advances

1. Introduction

Hydrogen is a clean, available alternative energy. Hydrolysis of alkaline sodium borohydride (NaBH₄) to produce hydrogen has been proposed for hydrogen delivery in portable applications due to the theoretically high hydrogen storage capacity (10.8 wt%). Active catalysts for hydride hydrolysis have included Co, Ni, Co and Ni borides,^{1,2} Ru,³ Pt,⁴ CoO and Cu₂O.^{5,6}

Recently, a large number of bimetallic catalysts, such as Pd–Cu/C, Pd–Ni/Ni foam,⁷ Ag–Pd⁸ and Au–Ag⁹ have been prepared by galvanic replacement, in which a non-noble metal with a lower potential is replaced by a noble metal to form the bimetallic material. In addition, the existence of the reduced surface can induce the generation of oxygen vacancies¹⁰ while the presence of oxygen vacancies in the catalysts can facilitate many redox reactions due to the decrease in work function of the materials.^{11,12} To our knowledge little has been reported on the synthesis of hydrolysis catalyst with oxygen defects using a reductive base metal as the precursor for galvanic replacement.

Kinetics study on NaBH₄ hydrolysis to produce hydrogen has extensively focused on the calculation and comparison of

activation energies over catalysts.^{13,14} Catalytic activity of catalysts, however, is influenced by internal and external diffusion as well as catalytic capacity of active site. In this case, their results for NaBH₄ hydrolysis may be more reasonable if the effect of mass transfer limitation in the solution is considered to determine real catalytic properties of catalysts.

In our previous study,¹⁵ we reported on the catalytic activity and stability of a Ru–RuO₂/C catalyst with oxygen vacancies for sodium borohydride hydrolysis. Although the catalyst showed promising activity, the source of the high catalytic activity and intrinsic activity capacity of Ru–RuO₂/C remained unclear. In the present study a series of Ru–RuO₂/C catalysts were prepared by galvanic replacement and characterized to investigate the formation of RuO₂ with the oxygen vacancies as well as Ru–RuO₂/C reduced, RuO₂/C and Ru supported on Ni foam (Ru/Ni foam). Under the conditions that the effect of mass transfer was eliminated, intrinsic activation energies of these catalysts were also calculated to compare real catalytic activity of Ru supported catalysts. This work is of great importance for the controllable preparation and reliable comparison of hydrolysis activity of heterogeneous catalysts.

2. Material and methods

2.1 Preparation, characterization and evaluation of catalytic materials

Ru–RuO₂/C was prepared by the method described previously.¹⁵ In a typical synthesis, the precursor Ni/C was prepared by hydrothermal synthesis (see ESI†). The as-prepared sample was dried in vacuum at 333 K for 5 h. Prior to characterization of the

^aDepartment of Chemical and Biochemical Engineering, College of Chemistry and Chemical Engineering, National Engineering Laboratory for Green Chemical Productions of Alcohols-Ethers-Esters, Xiamen University, Xiamen 361005, PR China. E-mail: yunhuali@xmu.edu.cn

^bDepartment of Chemical and Biological Engineering, University of British Columbia, 2360 East Mall, Vancouver, BC, V6T 1Z3 Canada

† Electronic supplementary information (ESI) available. See DOI: 10.1039/c6ra00747c

Ni/C, the dried sample was calcined at 573 K for 3 h. To obtain the RuO₂-based catalyst, the uncalcined Ni/C (0.3 g) was impregnated in an aqueous solution of RuCl₃ (25 mL, 9.64 mmol L⁻¹) at 323 K, filtered, dried and calcined 653 K for 3 h. If no specification is made, Ru-RuO₂/C denotes the sample treated for 18 h by the galvanic replacement reaction. For comparison, RuO₂/C and Ru/Ni foam (Ni foam was from Changsha Lyrun New Material Co. Ltd.) were also prepared from directly impregnating carbon and Ni foam support,⁷ respectively, as well as Ru-RuO₂/C reduced in H₂ atmosphere.

X-ray diffraction (XRD) of the catalysts was performed on a Rigaku Ultima-IV diffractometer equipped with a Cu K α radiation. X-ray photoelectron spectroscopy (XPS) tests were measured with the PHI Quantum 2000 Scanning ESCA Microprobe equipment. Temperature-programmed reduction (TPR) was performed using a conventional TPR apparatus. Electron spin resonance (ESR) was carried out using a Bruker EMX-10/12 Spectrometer at 90 K. Scanning electron microscope (SEM) images of original Ni foam and Ru/Ni foam were acquired with a Hitachi S-4800 FE-SEM. The elemental analysis of the samples was conducted on inductive couple plasma (ICP). The surface area of catalysts was determined *via* the N₂ adsorption-desorption isotherm method at 77 K using a Micromeritics TriStar II 3020 and the BET (Brunauer-Emmett-Teller) method. The pore size was calculated using the BJH (Barrett-Joyner-Halenda) method. Prior to the analyses, the samples were out-gassed at 523 K for 3 h to eliminate volatile adsorbates on the surface.

In a typical procedure for sodium borohydride hydrolysis, 0.01 g Ru-RuO₂/C (0.05 g Ru/Ni foam used because of lower reaction activity) was added into a 25 mL flask and then 5 mL alkaline NaBH₄ aqueous solution was introduced into this flask. Hydrogen generated during reaction process was collected into a gas collecting bottle (1 L), which has a minimum scale of 25 mL and an error of 5.0%.

2.2 Mass transfer calculations

Internal diffusion rate might directly affect catalytic performances for NaBH₄ hydrolysis reaction. Herein, the Wheeler-Weisz group was used to investigate the influence of internal mass transfer and defined as follows.¹⁶⁻¹⁹

$$\eta\phi^2 = \frac{r_{\text{obs}}R^2}{D_{\text{eff},i}C_s} \left(\frac{n+1}{2} \right) \quad (1)$$

where R is the diameter of pellet catalysts used in hydrolysis reaction process, which was detected through OMEC LS-908 type Laser Particle Size Analyzer. A general relationship between the effective diffusivity ($D_{\text{eff},i}$) and the pore diffusivity (D_p) is determined by parallel pore model.^{16,18,20}

$$D_{\text{eff},i} = \frac{\varepsilon}{\tau} D_p \quad (2)$$

ε is the porosity, which can be measured by BET method. τ is the tortuosity factors, which is influenced by temperature, adsorbate density and the diffusion mode and so on.²¹ A tortuosity factor for typical porous catalysts, 2, was used in this work. The diffusion coefficient, D_p , in the pores was calculated according

to a combination of the Knudsen diffusion coefficient (D_k) and the bulk diffusion coefficient ($D_{b,i}$). As for equimolar counter diffusion, D_p is defined according to the literature (eqn (3)).²²

$$\frac{1}{D_p} = \frac{1}{D_k} + \frac{1}{D_{b,i}} \quad (3)$$

Among them, D_k can be calculated from eqn (4)

$$D_k = 48.5D_p \sqrt{\frac{T}{M_i}} \quad (4)$$

On the other hand, Majumder *et al.*²³ studied mass transport through carbon nanotube membranes with ~ 7 nm pore diameter and found that ionic diffusion through the carbon nanotube (CNT) membranes is close to bulk diffusion expectations and electrostatically influenced by a charged carboxyl functionality at the CNT entrance. In our work, Ru-RuO₂/C treated in RuCl₃ solution was functionalized by a large number of hydrophilic groups. This implied that reactant ion, BH₄⁻, diffusion in Ru-RuO₂/C is similar to that in the literature. Therefore, the Knudsen diffusion coefficient of NaBH₄ in the pore of Ru-RuO₂/C can be obtained with two methods: (1) the conventional calculation for the gas phase according to eqn (4); (2) the Knudsen diffusion coefficient was regarded as the bulk diffusion²³ to simplify calculation. Eqn (3) was changed into eqn (5).

$$\frac{1}{D_p} = \frac{2}{D_{b,i}} \quad (5)$$

The bulk diffusion coefficient, $D_{b,i}$, was 3.63×10^{-5} cm² s⁻¹ estimated from experimental result in alkaline NaBH₄ solution.²⁴ Thus, the diffusion coefficient D_p in the pores of catalysts can be calculated according to eqn (3) or (5), respectively.

3. Results and discussion

3.1 Catalytic hydrolysis reaction of sodium borohydride

The catalytic activity of the catalysts prepared by galvanic replacement was determined for the hydrolysis of NaBH₄ and further was normalized by the metal amount in the catalysts

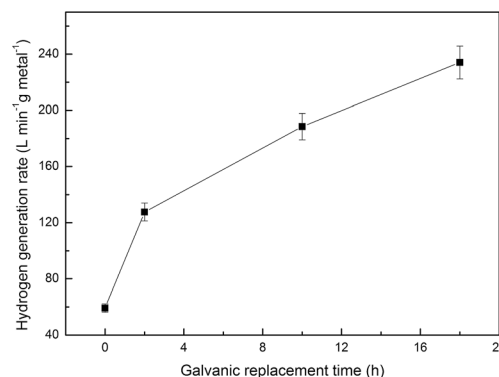


Fig. 1 Hydrolysis activity of NaBH₄ on Ru-RuO₂/C at different treatment time.

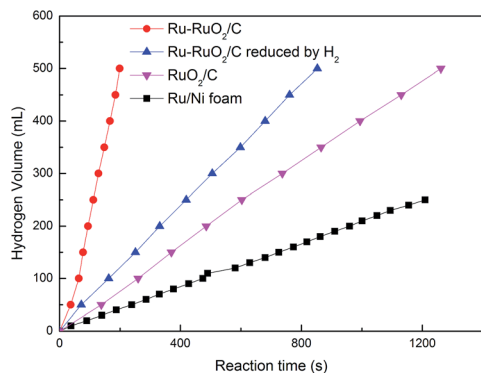


Fig. 2 Hydrolysis activity of NaBH_4 on different catalysts.

(Fig. 1). As shown in Fig. 1, hydrogen generation rates of the catalysts increased with increased galvanic replacement time, *i.e.* in the order of Ni/C precursor < Ru-RuO₂/C treated for 2 h < that treated for 10 h < that treated for 18 h. In comparison with Ru-RuO₂/C, Ru-RuO₂/C reduced, RuO₂/C and Ru/Ni foam present the lower hydrolysis activity (Fig. 2). To understand the change of catalytic activity of catalysts, a series of characterizations were conducted.

3.2 Characterization of catalysts

Ru/Ni foam. Table 1 demonstrated the textural characteristics of the materials. During impregnating and reducing process, the pore size and surface area of a series of Ru supported carbon change slightly except for Ru/Ni foam. Fig. 3 showed XRD patterns of Ni foam and Ru supported on Ni foam. Only diffraction peaks of Ni metal were found on Ni foam. After impregnating ruthenium precursor solution, NiO (101) is generated because of the dissolution of partial Ni foam and re-deposition. At the same time, a distinct peak was observed between Ru (002) and Ni (111) during the impregnation process, indicating the formation of a composite composed of metal Ru and Ni. XPS results (Fig. 4 and S1†) showed that Ru/Ni foam has the lower binding energy of Ru 3p than Ru-RuO₂/C catalysts. This further indicated that more Ru metal exists over Ru/Ni foam. In addition, H₂-TPR result showed that a few Ru oxide species are reduced as well as a large amount of Ni oxide species over Ru/Ni foam. And the addition of Ru contributes to the reduction of NiO over Ru/Ni foam compared with Ni foam (Fig. 5). Combining with SEM micrographs and EDX analysis of

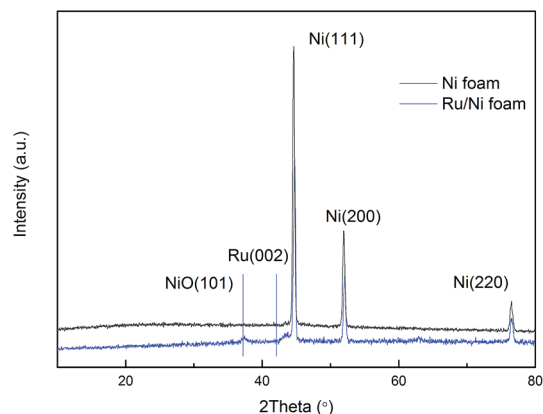


Fig. 3 XRD patterns of Ni foam and Ru/Ni foam.

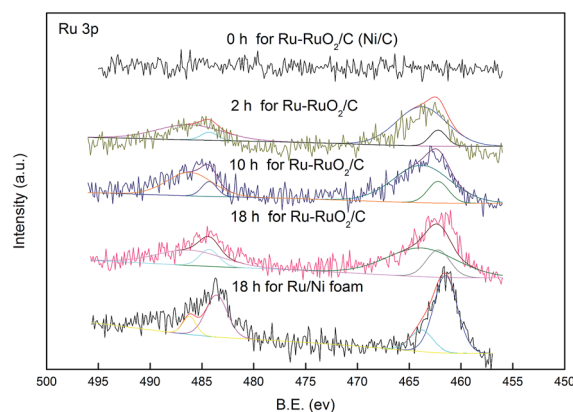


Fig. 4 XPS spectra of Ru 3p for different catalysts.

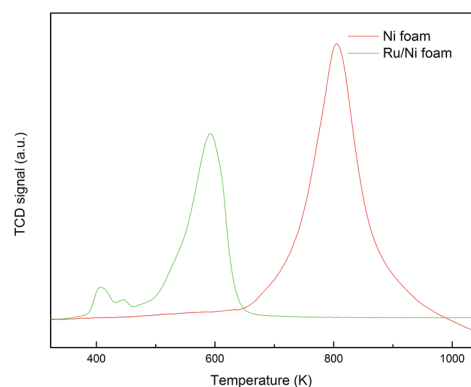


Fig. 5 H₂-TPR of Ni foam and Ru/Ni foam.

Table 1 The physiochemical structure of the materials

Catalyst	BET surface area (m ² g ⁻¹)	Pore size (nm)
Ru-RuO ₂ /C for 0 h (Ni/C)	1315.02	4.25
Ru-RuO ₂ /C for 2 h	1442.80	3.94
Ru-RuO ₂ /C for 10 h	1476.14	3.90
Ru-RuO ₂ /C for 18 h	1155.69	4.28
Ru-RuO ₂ /C reduced	1182.82	3.84
RuO ₂ /C	1429.32	4.11
Ru/Ni foam	13.79	23.09

Ni foam and Ru/Ni foam (Fig. 6), we believe that most of surface Ni and Ru oxide species interact with a composite consisting of Ru and Ni and exist in the form of a large number of nanoplates on Ni foam support.

Ru-RuO₂/C catalysts. Ni species in the form of Ni and NiO were highly dispersed over Ni/C (Fig. 7 and S1†). During the subsequent galvanic replacement process, the adsorbed precursor RuCl₃, with higher potential than the Ni species, reacts with the

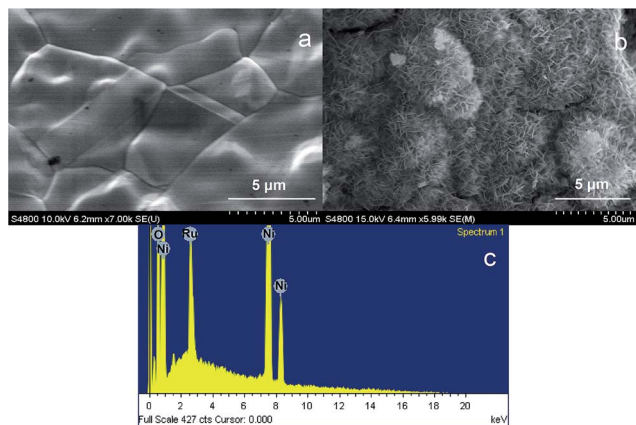


Fig. 6 SEM micrograph and EDX analysis of Ni foam and Ru/Ni foam. (a) Ni foam, (b) Ru/Ni foam and (c) EDX of Ru/Ni foam.

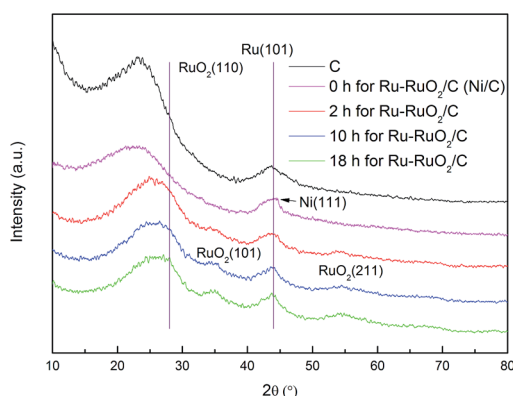


Fig. 7 XRD patterns of C and Ru–RuO₂/C at different galvanic replacement time.

nano-particle nickel because nickel has a higher reduction ability than the carbon support. The evolution of the adsorbed RuCl₃ into ruthenium oxide with oxygen vacancies was investigated by changing the galvanic replacement time.

In the XRD patterns of Fig. 7, diffraction peaks at 23.7° and 43.9° are attributed to reflections from carbon (JCPDS: 46-0945). The characteristic peaks at 28.0°, 35.1° and 54.3° correspond to (110), (101) and (211) reflections from rutile RuO₂ (JCPDS: 40-1290) while the diffraction peaks at 44.5° and 44.0° are attributed to Ni (111) and Ru (101), respectively. As shown in Fig. 7, diffraction peak of Ni (111) over Ni/C (0 h for Ru–RuO₂/C) is observed in comparison with carbon by hydrothermal treatment. XPS spectrum (Fig. S1†) of Ni/C showed that NiO appears in accompany with Ni metal. The negligible diffraction peak in XRD pattern is due to the high dispersion of NiO on Ni/C. The nickel (111) disappears while RuO₂ is formed (Fig. 7) after galvanic replacement. With increased galvanic replacement time, diffraction peak of RuO₂ over Ru–RuO₂/C is also gradually prominent, indicating the RuO₂ increases with increased treatment time.

In comparison with Ni/C, the appearance of a Ru 3p signal from the XPS spectra (Fig. 4) was accompanied by the disappearance of the Ni 2p spectrum after galvanic replacement for 2 h. In addition, Fig. 8 showed the H₂-TPR results of Ru–RuO₂/C at

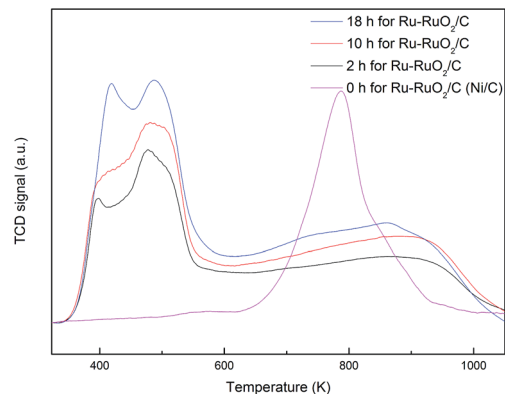


Fig. 8 H₂-TPR profiles of Ru–RuO₂/C at different galvanic replacement time.

different galvanic replacement time. As shown in Fig. 8, Ru–RuO₂/C has no obvious reduction peak for Ni oxide species after galvanic replacement for 2 h. These results indicate that the formation of RuO₂ is at the expense of both Ni metal and NiO in the initial stage of galvanic replacement. Since the standard reduction potential of Ni²⁺/Ni pair (−0.25 V, vs. standard hydrogen electrode, SHE) is lower than that of the RuCl₃/Ru pair (0.68 V, vs. SHE), RuCl₃ can be reduced to Ru by Ni under certain conditions. The produced Ru might be further oxidized in the solution.²⁵ We also impregnated commercial NiO powder with the RuCl₃ solution at 323 K. RuO₂ was observed by XRD (data not shown) and by XPS (Fig. S2†). Therefore, we conclude that Ru and RuO₂ on the Ru–RuO₂/C catalyst come from the reactions of Ni and NiO with RuCl₃ in the initial stage of galvanic replacement.

ICP analysis shows that the Ru loadings in Ru–RuO₂/C are 4.40, 5.23 and 6.13 wt% after treatment for 2, 10 and 18 h, respectively. H₂-TPR (Fig. 8) results demonstrated that the total amount of reduced oxygen species in Ru–RuO₂/C also increased gradually for the catalysts treated for 2, 10 and 18 h, respectively. The ratio of TPR peak area for Ru oxide species is almost equal and the total Ru loading is proximate for the samples for 2, 10 and 18 h, implying that both ruthenium oxide species and Ru metal increase simultaneously with increased galvanic replacement time. Since reactions between Ni species and RuCl₃ proceed

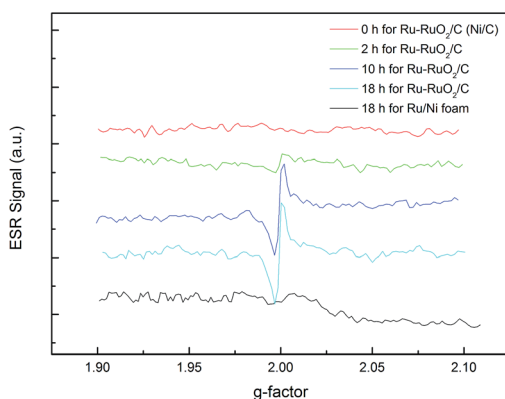


Fig. 9 Low-temperature ESR spectrum of catalysts in different treatment time.

within 2 h and the Ru and RuO₂ loading further increase with increased galvanic replacement time, the formation of Ru and RuO₂ results from the disproportionation of RuCl₃ adsorbed on catalysts under the conditions of the presence of air.^{26,27}

Fig. 9 showed low-temperature ESR spectra of different catalysts. The signals with characteristic *g*-factor values of 2.002 and 1.997 are identified as oxygen vacancies on RuO₂ (ref. 28) at magnetic fields of about 3360 G. There were no the other pronounced resonant features in the spectra. As shown in Fig. 9, the catalytic materials treated for 10 and 18 h, especially after 18 h, had obvious signals for oxygen vacancies.

In agreement with the content of oxygen vacancies, hydrogen generation rates of the catalysts increased with increased galvanic replacement time, *i.e.* in the order of Ni/C precursor < Ru–RuO₂/C treated for 2 h < that treated for 10 h < that treated for 18 h (Fig. 1). The consumption of Ni species accompanied with the formation of oxygen vacancies on RuO₂ occurred within 2 h. However, the highest catalytic activity occurs on Ru–RuO₂/C treated for 18 h. This is mainly because of continued disproportionation of RuCl₃ yielding an increased number of Ru and RuO₂ species with oxygen vacancies epitaxially grown on the catalyst. RuO₂ with oxygen vacancies can facilitate water decomposition, a rate-determining step for NaBH₄ hydrolysis,

while Ru metal acts as an active phase to dissociate NaBH₄. Thus, under the conditions that Ru metal and RuO₂ cocatalyze NaBH₄ hydrolysis, Ru–RuO₂/C shows the highest catalytic activity of sodium borohydride hydrolysis.

ESR spectrum presented no oxygen defects on Ru/Ni foam. In other words, Ru and Ni metal composite, rather than Ru and RuO₂ with oxygen vacancies, was obtained by Ni foam as a rich reductive support impregnated by Ru precursor solution. In comparison with Ru–RuO₂/C, Ru/Ni foam without oxygen defects has relative low catalytic activity for NaBH₄ hydrolysis to hydrogen. This is also further discussed in 3.3 section.

3.3 Intrinsic kinetic study

A Ru–RuO₂/C catalyst with oxygen vacancies showed the high catalytic activity in NaBH₄ hydrolysis. Herein, intrinsic kinetics of Ru–RuO₂/C was studied and compared with the Ni and Ru metal composites, Ru–RuO₂/C reduced and Ru/Ni foam, and the results from literatures. Fig. S3† presented the NaBH₄ hydrolysis reaction results over Ru–RuO₂/C at various stirring speed to check the effect of external diffusion on hydrolysis reaction. With increased stirring speed, the rate of hydrogen generated firstly increases²⁹ and then decreases. At the stirring speed higher than 200 rpm, hydrogen generation rate reached the

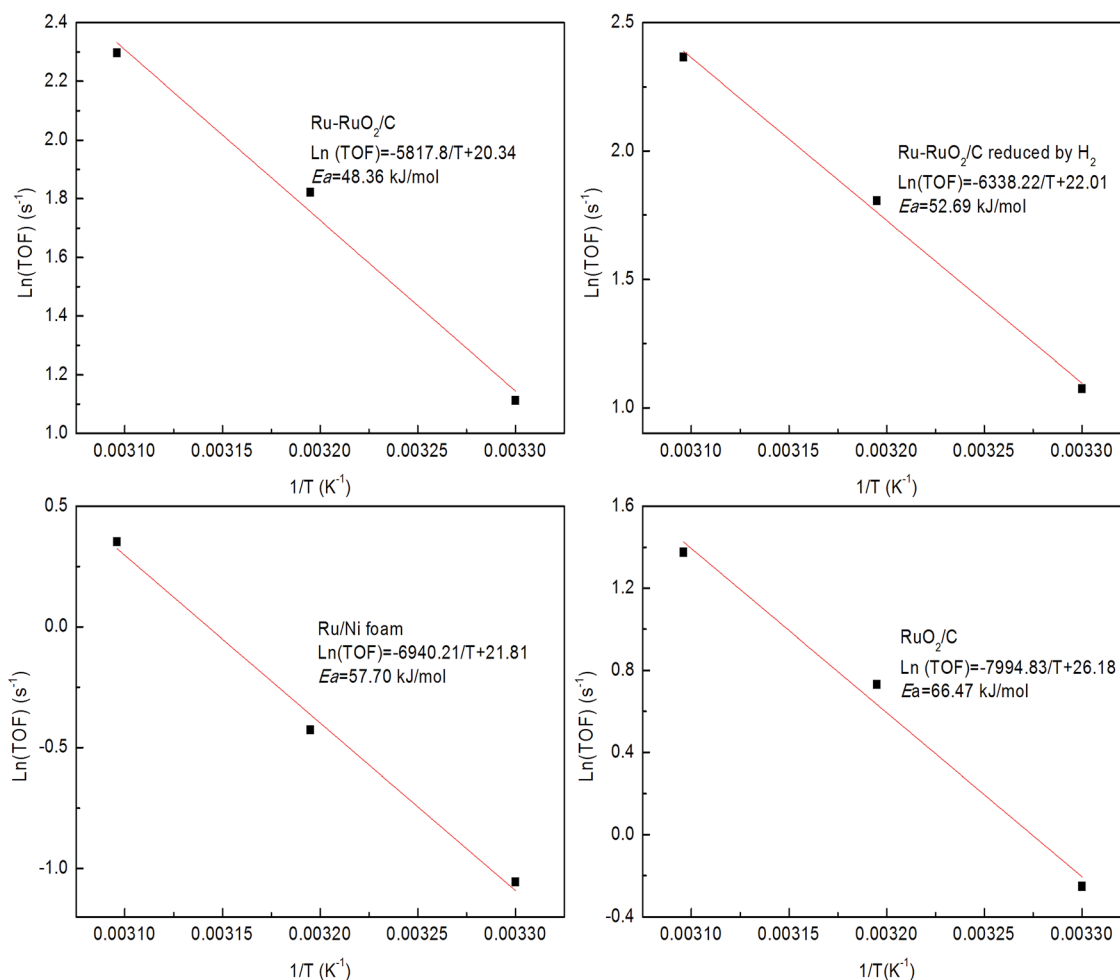


Fig. 10 Arrhenius plot obtained from TOF for different catalysts.

maximal value, indicating that external mass transfer limitation is almost completely eliminated in this case. At 300 rpm, the decreasing in reaction rate might be result from unexpected adhesion of catalysts to the upper wall of the flask at high stirring speed.

Influence of internal diffusion on hydrolysis reaction was further estimated over Ru–RuO₂/C. Calculation value of the Wheeler–Weisz group, based on the conventional gas phase or the assumption that the Knudsen diffusion coefficient is equal to the bulk diffusion, is 0.0048 or 0.0024, respectively. It is generally accepted that the effect of the internal mass transfer on the reaction rate can be neglected when the value of $\eta\phi^2$ is less than 0.1. In this work, the difference of the Wheeler–Weisz group on the basis of two methods derives from the Knudsen diffusion coefficient. At present, the accurate calculation for Knudsen diffusion coefficient of fluid component is still under way. However, since the possible calculation values of $\eta\phi^2$ were far away from 0.1, the influence of internal mass transfer on the hydrolysis reaction should be negligible over Ru–RuO₂/C. The porous structure of Ru–RuO₂/C reduced and RuO₂/C is similar to that of Ru–RuO₂/C (Table 1), so the effect of diffusion on activity over Ru–RuO₂/C reduced and RuO₂/C was also not prominent. With respect to Ru/nickel foam, the pore size is very large even though after it was modified by Ru (Table 1). In this case, the effect of internal diffusion is negligible.

Under the conditions that the reaction process is free from the external and internal mass transfer limitations, turnover frequency (TOF) was estimated by dividing the mole amount of hydrogen produced per second by the mole amount of metal on catalysts used. Arrhenius plots for TOF as a function of temperature was given in Fig. 10. The corresponding activation energy of catalysts was also presented in Fig. 10. As displayed in Fig. 10, Ru–RuO₂/C has the relative lower activation energy than Ru/Ni foam. When the apparent activation energy is not affected by mass transfer, the lower activation energy implies the relative higher catalytic activity of Ru–RuO₂/C than Ru/Ni foam. In contrast, most of activation energies from literatures are apparent results (Table 2) and they might be influenced by mass transfer. In this case, Ru–RuO₂/C showed a moderate activity.

Table 2 The comparison of activation energies of catalysts from literatures

Catalyst	Temperature (K)	E_a (kJ mol ⁻¹)	Ref.
Ni ₄₅ Au ₄₅ Co ₁₀	303–318	18.8	31
Ru/Ti ₃ C ₂ X ₂	298–313	22.1	32
Au ₂₀ Ni ₈₀ BNP	303–318	30.3	33
Co–Mo–B	293–323	43.7	14
Ni–B	303–333	~45–47	34
Ru/HMS	283–303	46.7	35
Co–P	303–323	47.0	36
NiB/capsule	303–333	49.3	37
Co–La–Zr–B	293–323	51.2	38
Ni–Co–P/ γ -Al ₂ O ₃	298–328	52.1	39
Ni–Ru/50WX ₈	288–348	52.7	40
Co–B/IR-120	273–353	66.3–81.7	41
Ru–RuO ₂ /C	303–323	48.4	This work

However, considering the pore diffusion limitation, true apparent reaction activation energies (E_t) are modified by a diffusion activation energy (E_d) term such that the observed apparent activation energy is given by $E_{ob} = (E_t + E_d)/2$.³⁰ Thus, more severe diffusion limitations might lead to the low apparent activation energies from those literatures or difficulty in comparison of catalytic results. Although some catalysts in the literatures reported were used in the form of nanoparticles for hydrolysis reaction, the effect of particle aggregation in the solution on internal mass transfer is still unclear. To reliably determine catalytic capacity of active site over heterogeneous catalysts, the intrinsic activation energies for hydride hydrolysis to hydrogen should be presented on the basis of elimination of mass transfer limitation. This was done for the first time in the present work.

4. Conclusions

The present study shows that the formation of a part of Ru and RuO₂ is at the expense of Ni and NiO and the other comes from the disproportionation of RuCl₃. RuO₂ with oxygen vacancies in Ru–RuO₂/C determines hydrolysis activity of sodium borohydride. In contrast, Ru/Ni foam without oxygen vacancies exhibits the low catalytic activity. Under the conditions eliminating internal and external diffusion, intrinsic activation energy obtained is, 48.36 kJ mol⁻¹, lower than that from Ru–RuO₂/C reduced, RuO₂/C and Ru/Ni foam. Ru–RuO₂/C with oxygen vacancies has the higher intrinsic catalytic activity than metal Ru and Ni composite. Since the apparent activation energies are affected by mass-transfer limitations, the comparison of real activity on hydrolysis catalysts should be conducted based on intrinsic activation energies.

Abbreviations

$\eta\phi^2$	Wheeler–Weisz group, dimensionless
r_{obs}	Apparent reaction rate, mol L ⁻¹ s ⁻¹
R	Thickness of wash-coat or diameter of the pellet and cylindrical catalysts, m
n	Reaction order
$D_{eff,i}$	Effective diffusion coefficient in the pores of the catalyst, m ² s ⁻¹
C_s	BH ₄ ⁻ concentration at the surface of catalyst, mol m ⁻³
D_p	The diffusion coefficient in the pores, m ² s ⁻¹
D_k	The Knudsen diffusion coefficient, m ² s ⁻¹
d_p	Pore diameter of catalyst, m
T	Temperature, K
M	Molecular weight of BH ₄ ⁻ species
$D_{b,i}$	The bulk diffusion coefficient of specie i, m ² s ⁻¹

Greek letters

ϵ	Void fraction (porosity) of catalyst bed, dimensionless
τ	Tortuosity factor, dimensionless

Acknowledgements

This work was supported by National Natural Science Foundation of China (Grant No. 21476188, 21106118).

Notes and references

- N. Patel and A. Miotello, *Int. J. Hydrogen Energy*, 2015, **40**, 1429–1464.
- N. Sahiner and A. O. Yasar, *Fuel Process. Technol.*, 2014, **125**, 148–154.
- H. Y. Ma and C. Z. Na, *ACS Catal.*, 2015, **5**, 1726–1735.
- C. Salameh, A. Bruma, S. Malo, U. B. Demirci, P. Miele and S. Bernard, *RSC Adv.*, 2015, **5**, 58943–58951.
- Y. Yamada, K. Yano and S. Fukuzumi, *Energy Environ. Sci.*, 2012, **5**, 5356–5363.
- H. Zhang, T. Ling and X. W. Du, *Chem. Mater.*, 2015, **27**, 352–357.
- Y. Li, L. Zhu, K. Yan, J. Zheng, B. H. Chen and W. Wang, *Chem. Eng. J.*, 2013, **226**, 166–170.
- L. Xu, Z. M. Luo, Z. X. Fan, S. J. Yu, J. Z. Chen, Y. S. Liao and C. Xue, *Chem.–Eur. J.*, 2015, **21**, 8691–8695.
- J. Lee, K. Han and D.-J. Jang, *Appl. Catal., A*, 2014, **469**, 380–386.
- X. Wang, N. M. Perret, J. J. Delgado, G. Blanco, X. Chen, C. M. Olmos, S. Bernal and M. A. Keane, *J. Phys. Chem. C*, 2013, **117**, 994–1005.
- M. V. Ganduglia-Pirovano, A. Hofmann and J. Sauer, *Surf. Sci. Rep.*, 2007, **62**, 219–270.
- M. T. Greiner, L. Chai, M. G. Helander, W. M. Tang and Z. H. Lu, *Adv. Funct. Mater.*, 2012, **22**, 4557–4568.
- S. G. Peng, X. J. Fan, J. Zhang and F. Y. Wang, *Appl. Catal., B*, 2013, **140**, 115–124.
- D. D. Ke, Y. Tao, Y. Li, X. Zhao, L. Zhang, J. D. Wang and S. M. Han, *Int. J. Hydrogen Energy*, 2015, **40**, 7308–7317.
- Y. Li, Q. Zhang, N. Zhang, L. Zhu, J. Zheng and B. H. Chen, *Int. J. Hydrogen Energy*, 2013, **38**, 13360–13367.
- H. R. Yue, Y. J. Zhao, L. Zhao, J. Lv, S. P. Wang, J. L. Gong and X. B. Ma, *AIChE J.*, 2012, **58**, 2798–2809.
- K. Arnby, A. Tornocrona, B. Andersson and M. Skoglundh, *J. Catal.*, 2004, **221**, 252–261.
- L. Ronchin and L. Toniolo, *Catal. Today*, 1999, **48**, 255–264.
- E. Crezee, B. W. Hoffer, R. J. Berger, M. Makkee, F. Kapteijn and J. A. Moulijn, *Appl. Catal., A*, 2003, **251**, 1–17.
- Z. G. Wang, S. L. Chen, J. N. Pei, A. C. Chen, J. H. Zhang, Z. M. Xu and J. B. Benziger, *AIChE J.*, 2014, **60**, 3267–3275.
- M. R. Bonilla and S. K. Bhatia, *J. Phys. Chem. C*, 2013, **117**, 3343–3357.
- J. von Rickenbach, F. Lucci, C. Narayanan, P. D. Eggenschwiler and D. Poulikakos, *Chem. Eng. J.*, 2015, **276**, 388–397.
- M. Majumder, N. Chopra and B. J. Hinds, *ACS Nano*, 2011, **5**, 3867–3877.
- M. Chatenet, M. B. Molina-Concha, N. El-Kissi, G. Parrour and J. P. Diard, *Electrochim. Acta*, 2009, **54**, 4426–4435.
- G. Chen, S. Desinan, R. Rosei, F. Rosei and D. Ma, *Chem. Commun.*, 2012, **48**, 8009–8011.
- Y. Guo, H. Li and H. Kameyama, *Chem. Eng. Sci.*, 2011, **66**, 6287–6296.
- D. V. Bavykin, A. A. Lapkin, P. K. Plucinski, J. M. Friedrich and F. C. Walsh, *J. Catal.*, 2005, **235**, 10–17.
- P. A. Osorio-Vargas, C. Pulgarin, A. Sienkiewicz, L. R. Pizzio, M. N. Blanco, R. A. Torres-Palma, C. Pétrier and J. A. Rengifo-Herrera, *Ultrason. Sonochem.*, 2012, **19**, 383–386.
- S. F. Lim, Y. M. Zheng, S. W. Zou and J. P. Chen, *Chem. Eng. J.*, 2009, **152**, 509–513.
- T. Zhang, J. Li, J. Liu, D. Wang, Z. Zhao, K. Cheng and J. Li, *AIChE J.*, 2015, **61**, 3825–3837.
- C. Jiao, Z. Huang, X. Wang, H. Zhang, L. Lu and S. Zhang, *RSC Adv.*, 2015, **5**, 34364–34371.
- X. Li, G. Fan and C. Zeng, *Int. J. Hydrogen Energy*, 2014, **39**, 14927–14934.
- X. Wang, S. Sun, Z. Huang, H. Zhang and S. Zhang, *Int. J. Hydrogen Energy*, 2014, **39**, 905–916.
- Z. J. Wu, X. K. Mao, Q. Zi, R. R. Zhang, T. Dou and A. C. K. Yip, *J. Power Sources*, 2014, **268**, 596–603.
- S. Peng, B. Pan, H. Hao and J. Zhang, *J. Nanomater.*, 2015, **2015**, 1–11.
- Y. Wang, K. Qi, S. Wu, Z. Cao, K. Zhang, Y. Lu and H. Liu, *J. Power Sources*, 2015, **284**, 130–137.
- Y. Chen, Y. Shi and Y. Wang, *Int. J. Energy Res.*, 2015, **39**, 634–642.
- M. H. Loghmani and A. F. Shojaei, *Energy*, 2014, **68**, 152–159.
- Z. Li, H. Li, L. Wang, T. Liu, T. Zhang, G. Wang and G. Xie, *Int. J. Hydrogen Energy*, 2014, **39**, 14935–14941.
- C.-H. Liu, B.-H. Chen, C.-L. Hsueh, J.-R. Ku, M.-S. Jeng and F. Tsau, *Int. J. Hydrogen Energy*, 2009, **34**, 2153–2163.
- Y.-H. Chen and C.-Y. Pan, *Int. J. Hydrogen Energy*, 2014, **39**, 1648–1663.